PCCP

PAPER

View Article Online
View Journal | View Issue

Cite this: *Phys. Chem. Chem. Phys.*, 2017, **19**, 1526

Surface chemistry and density distribution influence on visible luminescence of silicon quantum dots: an experimental and theoretical approach†‡

Ateet Dutt,[a] Yasuhiro Matsumoto,*[b] G. Santana-Rodríguez,*[a] Estrella Ramos,*[a] B. Marel Monroy[a] and J. Santoyo Salazar[c]

The impact of the surface reconstruction of the density distribution and photoluminescence of silicon quantum dots (QDs) embedded in a silicon oxide matrix (SiO_x) has been studied. Annealing treatments carried out on the as-deposited samples provoked the effusion of hydrogen species. Moreover, depending on the surrounding density and coalescence of QDs, they resulted in a change in the average size of the particles depending on the initial local environment. The shift in the luminescence spectra all over the visible region (blue, green and red) shows a strong dependence on the resultant change in the size and/or the passivation environment of QDs. Density functional theoretical (DFT) calculations support this fact and explain the possible electronic transitions (HOMO–LUMO gap) involved. Passivation in the presence of oxygen species lowers the band gap of Si_{29} and Si_{35} nanoclusters up to 1.7 eV, whereas, surface passivation in the environment of hydrogen species increases the band gap up to 4.4 eV. These results show a good agreement with the quantum confinement model described in this work and explain the shift in the luminescence all over the visible region. The results reported here offer vital insight into the mechanism of emission from silicon quantum dots which has been one of the most debated topics in the last two decades. QDs with multiple size distribution in different local environments (band gap) observed in this work could be used for the fabrication of light emission diodes (LEDs) or shift-conversion thin films in third generation efficient tandem solar cells for the maximum absorption of the solar spectrum in different wavelength regions.

Received 28th October 2016,
Accepted 28th November 2016

DOI: 10.1039/c6cp07398k

www.rsc.org/pccp

Introduction

Ever since visible emission from Si nanostructures was observed in the early 1990s,[1,2] it highlighted that the basic properties of Si nanoparticles (NPs) differ spectacularly from their counterparts (bulk structure). It opened up the possibility of using Si nanoparticles (NPs) or quantum dots (QDs) for integrated optoelectronic applications. Generally, in the case of NPs, the dimensions could be in the range of up to 100 nm, whereas, in the case of QDs they have to have particle radii of <5 nm for exhibiting the quantum confinement effect (QCE). Despite that, much productive investigation has been made on nanocrystalline silicon; still, compatibility to manufacture silicon thin films with the potential of emitting in the visible region with precise knowledge of the emission mechanism is left with constraints. However, till now some hypotheses have been put forth to explain the emission mechanism.[3,4] Knowledge and advancement in this aspect could result in the development of optoelectronic devices compatible with the current silicon based microelectronics industry[5] and keeping in mind the non-toxic nature of silicon as well, the obtained luminescence could also be used in the area of *in vivo* biological sample analysis.[6,7]

There are numerous kinds of mechanisms known for the emission from silicon thin films. Firstly, the quantum confinement effect, where the band gap of the material tends to increase with the reduction in the size of the QDs, depends on the relation mentioned in eqn (1)[8]

$$E = 0.925 + \frac{3.73}{d^{1.39}} + \frac{0.881}{d}. \quad (1)$$

[a] *Instituto de Investigaciones en Materiales, Universidad Nacional Autónoma de México, Coyoacán, México City, 04510, Mexico. E-mail: gsantana@iim.unam.mx, eramos@iim.unam.mx*

[b] *SEES, Electrical Engineering Department, Centro de Investigación y de Estudios Avanzados del IPN, México City, 07360, Mexico. E-mail: ymatsumo@cinvestav.mx*

[c] *Departamento de Física, Centro de Investigación y de Estudios Avanzados del IPN, México City, 07360, Mexico*

† The authors would like to dedicate this article to one of the co-authors: Dr Betsabée Marel Monroy Peláez. Very sadly after a long battle with cancer her soul departed us on the 16th of October 2016 at the age of 38.

‡ Electronic supplementary information (ESI) available: Absorption spectra, profilometry and frontier molecular orbital diagrams of (H, H, H) clusters and (OH, OH, and OH) clusters for Si_{29}. See DOI: 10.1039/c6cp07398k

Eqn (1) shows the relationship between the peak photon energy (E in eV) and the nanocrystal diameter (d in nm) which gives good agreement with experimental data for nanocrystals with diameters greater than 2 nm. This relation is also valid for the particles passivated by hydrogen and oxygen, respectively. Secondly, when the silicon nanoparticles are embedded in an amorphous matrix (SiO_x), the luminescence could also originate from various defects related to the Si–H (hydrides) bonding states, oxygen deficiency centres ($\equiv$Si–Si$\equiv$), non-bridging oxygen centres ($\equiv$SiO), surface trapped excitons and/or dangling bonds giving rise to intermediate levels inbetween the band energy states.[9–15] Even in some cases, PL is likewise attributed to the surface passivation caused by Si=O species on the nanoparticle surface.[16] We have performed some DFT simulations to analyse the effect of surface passivation in this paper. It is important to mention at this point that the term passivation corresponds to the stability of the QD's surface due to the saturation of the free terminal bonds with oxygen and/or hydrogen species (present work).

In our previous reports, we have shown visible emission from the as-deposited samples (broad and homogenous distribution of particles) and the mechanism of white luminescence was correlated with the quantum confinement effect by varying the deposition conditions using HW-CVD.[17–19] In other recently published reports, we have also shown the variation in colour emission from blue to green and then, red colour depending on the thickness of samples.[19]

In this report, we perform an annealing of the sample to observe the differences appearing in the morphology of various positions of the same sample and correlate the annealing aftereffect on the PL emission. As we know, while working with QDs, even a small variation in the size of the particle and thus, the band gap of the material could result in different emission energies and the same is clear from eqn (1). In comparison to our earlier published works, in the present work, annealing in the atmosphere of nitrogen gas (N_2) caused the effusion of hydrogen in thin films and even more due to the differences in the local environment associated with the density of particles and their surface passivation, it caused evident differences in the local density and distribution of nanoparticles in the matrix.

Foremost, in this article, in comparison to the old literature,[9–16] different phenomena related to diverse colour emissions have been illustrated. The as-grown sample showed the presence of particles in the size regime of 2–5 nm with bright white emission depending on the similar passivation. Annealing in a low temperature atmosphere triggered different colour emissions due to the differences appearing in the passivation of nanoparticles irrespective of the same size regime. Furthermore, annealing at higher temperature provoked the red emission due to modifications appearing in the passivation of the nanoparticles and the increase in the average size of nanoparticles. Together with the experimental results obtained, additional theoretical studies were made using DFT calculations on different Si clusters with 17, 29, 35 and 87 atoms to reveal the effect of surface passivation of oxygen/hydrogen species on the surface of QDs. The results showed a significant band gap change from 1.7 eV to 4.4 eV depending on the passivation or size/stabilization of QDs and presented an excellent correlation with the QCE model. As per our knowledge, primarily in this report, a brief description of different colour emissions from silicon thin films including the size and/or the passivation effect on visible luminescence *via* combining experimental and DOS studies has been presented.

Due to their improved absorption and tunable band gap, quantum dots are great candidates for the fabrication of optoelectronic devices and distinct biological applications. This particular thin film configuration can be used in tandem solar cells as it helps a lot to enhance the photocurrent response and increase the probability of light harvesting.[20] In a nutshell, in this study, this approach has been followed to find the structural and morphological differences appearing in the annealed sample by using AFM, SEM, XRD, and FTIR and hence, to locate the mechanism of the resulting emission for future applications in device fabrication.

Materials and methods

Materials

The hot wire chemical vapour deposition system used for the deposition consists of a stainless-steel chamber and the complete details of the equipment have been described elsewhere.[21] The system was evacuated to a high vacuum of around 10^{-4} Pa using a turbomolecular pump (Varian model V-550). Tungsten (W) was used as a filament material, and the distance between the filament and the substrate was maintained at 5 cm. The flow rates of the source gases were kept at 5 sccm (standard cubic centimetre per minute) for both hydrogen (H_2) and pure silane (SiH_4). The oxygen (O_2) flow was maintained at 0.5 sccm for 40 minutes. After allowing the flow of all four gases, the pressure in the chamber was maintained at 0.1 Torr using a throttle valve and a pressure-sensing system (Baratron, model-253B-20-40-2). Two kinds of substrate materials were used, including Corning Glass 2497C and p-type crystalline silicon. Heat treatment experiments were carried out for one of the samples deposited on a silicon substrate at filament temperature (T_{fil}) = 1800 °C and substrate temperature (T_{subs}) = 200 °C for 40 minutes. The sample was cut into different parts, and annealing in a nitrogen atmosphere was performed at two different temperatures, 550 °C (termed low temperature annealing) and 950 °C (termed high temperature annealing) for the same time duration (60 minutes). Comparison has been made between the as-deposited and annealed samples, using various characterization techniques.

Methods

Photoluminescence (PL) spectra were obtained using a Kimmon Koha He–Cd laser with an excitation wavelength of 325 nm, and the transmittance spectrum was recorded using a Shimadzu UV-2401PC. Transitions among phases were analysed by X-ray diffraction, using an XRD-Siemens model D5000 configured with Cu-Kα radiation (λ = 1.5418 Å) generated at 25 mA and 35 kV. Diffraction patterns were found in (θ–2θ) configuration

from 20–80° (2θ) by using a step of 0.02° every 10 s. Fourier transform infrared (FTIR) spectra were recorded in absorption mode with a resolution better than 1 cm^{-1}, within the range of 400 to 4000 cm^{-1} using a Nexus 470 Thermo-Nicolet spectrometer. AFM analyses were performed, at different locations of the sample to observe the morphological changes appearing in the various parts of the sample using an NT-MDT model. A FESEM-Carl Zeiss-AURIGA (Field Emission Scanning Electron Microscope) was used to capture the morphologically related micrographs at 2.0 kV. A Transmission Electron Microscope, TEM (JEOL-JEM-2010), was used to obtain the bright images at 200 kV with a wavelength, λ = 0.027 Å, and a camera distance, L = 20 cm.

Computational details

Density functional approximation[22–24] as implemented in Gaussian 09[25] was used for all the calculations. Full geometry optimization without symmetry constraints was obtained with the Perdew and Wang 1991 gradient-corrected correlation functional[26] (B3PW91) and the 6-31G(d,p) basis set[27] within the Density Functional Theory (DFT) framework.[28] This model was selected following the same methodology as in previous work.[29]

Different starting geometries were used for the geometry optimization, considering that there are two possible replacements of the H atoms: (i) in the terminal silicon atoms that are bonded to only one hydrogen atom (Si–H), or (ii) in the silicon atoms that are bonded to two H atoms ($Si–H_2$). To see the effect on Si clusters with different sizes and passivation environments, we have used the arrangement as in the form: Si_n (X, Y, Y') where n = 17, 29, 35 and 87.[29] And the structural order of X, Y, Y' has been rearranged in five different forms such as: (i) H, H, H ($Si_{29}H_{36}$), (ii) H, H, OH ($Si_{29}OH_{12}H_{24}$), (iii) H, OH, OH ($Si_{29}OH_{24}H_{12}$), (iv) OH, OH, OH ($Si_{29}OH_{36}$) and (v) OH, H, H ($Si_{29}OH_{12}H_{24}$). These notations are illustrated in Scheme 1. After optimization, the substituted structures that we found are slightly distorted on the corresponding structures passivated with hydrogen atoms. The Connolly surface was used to estimate the size of the Si-QDs.[30]

The Density of States (DOS) for all the systems under study was obtained in the framework of DFT-GGA utilizing the PW91 exchange and correlation functional in the DMol3 package with a double numerical basis set implemented in the Materials Studio software suite 2016. The cluster geometry corresponds to the optimized Gaussian structure described above. Optimized geometries, band-gap values, DOS, molecular orbitals, and electrostatic potential onto electron density were used as the tools to analyse the electronic properties of the clusters. The aim of the simulations carried out in the present work is to support the experimental results obtained. Hence, different models were simulated providing the passivation of the nanoclusters using oxygen and hydrogen species. Furthermore, the resulting effect of the passivation on the size and electronic properties has been discussed briefly in the text.

Results and discussion

Photoluminescence spectra

Fig. 1 depicts the normalized PL spectra of the sample before and after low temperature annealing at different positions of the sample surface. The as-deposited sample showed an almost identical white-blue colour emission at 470 nm (2.6 eV) all over the sample with some differences in the intensity of the emission when the laser scan was made at different spots. The differences in PL intensity are associated with the differences in the QD density in the sample, with bright spots corresponding to regions of high density of QDs. Additionally, the absorption spectra of the as-deposited sample (on glass) have been provided in Fig. S1 (ESI‡). In the present case, the absorption edge appears in the lower wavelength (or higher energies) region which remarks the broadening of the band gap which could be responsible for the white emission from the as-deposited sample.

Nevertheless, after low temperature annealing, as the laser was scanned over the surface of the sample, different colour emissions were observed by the naked eye at room temperature (the inset shows the colour emission by pointing the He–Cd laser at different zones of the sample). One of the emissions obtained after annealing was almost identical to that from the as-deposited sample at 470 nm (2.6 eV), whereas, other two of them showed enormous variation in the colour emission and

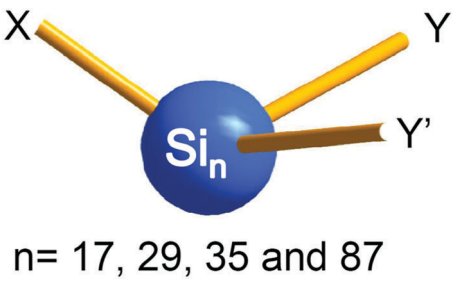

Scheme 1 Representation of the model used for theoretical calculations. The surface substituents X, Y and Y' have been rearranged in five different forms such as: (i) H, H, H ($Si_{29}H_{36}$), (ii) H, H, OH ($Si_{29}OH_{12}H_{24}$), (iii) H, OH, OH ($Si_{29}OH_{24}H_{12}$), (iv) OH, OH, OH ($Si_{29}OH_{36}$) and (v) OH, H, H ($Si_{29}OH_{12}H_{24}$).

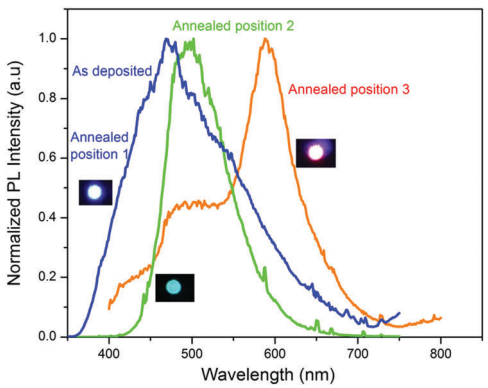

Fig. 1 PL spectra of the sample before and after low temperature annealing; the insets show the three emission colours observed at room temperature.

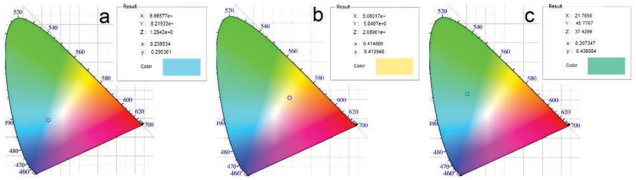

Fig. 2 CIE diagram for three emissions observed for the annealed samples in Fig. 1; (a) corresponds to position 1, (b) corresponds to position 2 and (c) corresponds to position 3, respectively.

were obtained at 498 nm (2.4 eV) and 588 nm (2.1 eV), respectively. From the absorption spectra in the visible region of the as-grown sample (Fig. S1, ESI‡), it is clear that the combination of band gaps (blue, green) could finally result in white emission. However, after low temperature annealing, the red shift could be due to the trapping of exciton pairs corresponding to the energy levels as mentioned in one of our previous reports.[17]

Also, to identify the true colour emissions from the sample, the CIE software (Commission International de l'Eclairage) Chromaticity diagram has been used.[18] Fig. 2 shows the real colour emission obtained from the sample along with the coordinate values (x and y) for the corresponding spectra. Fig. 2(a) is equivalent to position 1 and in this case, the values of coordinates are x = 0.239534 and y = 0.295361. Fig. 2(b) corresponds to position 2, and in this case, the values of coordinates are x = 0.207347 and y = 0.436084, whereas Fig. 2(c) corresponds to position 3 and has the coordinate values x = 0.414806 and y = 0.413948. The obtained results showed good colour concordance with the experimental results shown in Fig. 1.

FTIR analysis

Fig. 3 shows the infrared absorption spectral (FTIR spectroscopy) results related to the sample before and after low temperature annealing. It was intended to do the measurement at different points, after low temperature annealing (by reducing spot size), of the sample to spot the differences triggering the emission in diverse colour regions related to the bonding peaks. However, the same kind of response was observed and hence, only one spectrum is shown in Fig. 3. The spectra, in general, exhibited absorption peaks related to (i) Si–O out-of-plane rocking, (ii) Si–Si, (iii) Si–H wagging, (iv) Si–O bending, (v) Si–H bending and (vi) Si–O stretching in-phase and out-of-phase modes. From the spectra it can be observed that Si–H wagging absorption at 620 cm^{-1} decreased effectively by hydrogen effusion because of annealing treatment.

On the other hand, the absorption band at 800 cm^{-1} corresponding to the Si–O bond acquired an overall increased intensity after annealing.[31,32] Si–H bending at 880 cm^{-1} diminished totally after the annealing process. Hence, it can be illustrated that the absorbance intensity of the bonds related to oxygen increases with annealing treatment. It implies that the silicon in the film either might be oxidized by the oxygen from air in the atmosphere or from the substrate effect.[31] The FTIR results confirm the surface or surrounding change occurred due to low temperature annealing.

For the low temperature annealed sample, no significant differences were observed in the peaks for the measurements performed at different points and this remarks that apart from various defect states earlier mentioned in Section 1, which could be easily detected using FTIR spectroscopy, the mechanism of emission is different, or it could be related to the morphological structure. Profound structural and morphological studies have been conducted using XRD, SEM, TEM, and AFM characterization and more details are provided in the subsequent sections.

XRD analysis

Fig. 4 illustrates the XRD pattern of the sample before and after low temperature annealing. Here as well, it was intended to do the measurement in different regions of the annealed sample, but as the measurements have been performed using the grazing angle (covering a vast area of the sample), it was not conceivable to do the measurements at different points. From the pattern, the presence of three distinguished peaks for Si at 28.4, 47.4 and 56.1° analogous to (111), (220) and (311), respectively, could be observed for both the as-deposited and annealed samples. The only difference observed for the annealed sample was at the specific plane (311), which could be clearly seen from Fig. 4.

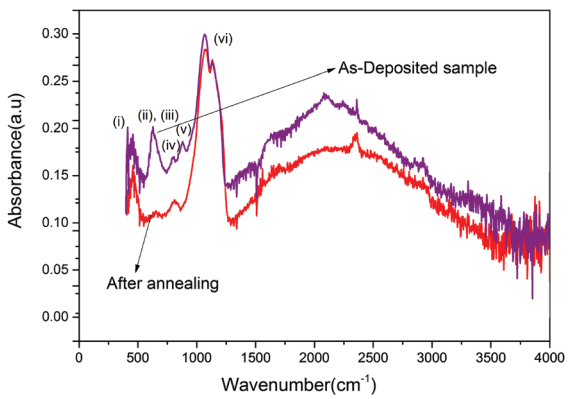

Fig. 3 FTIR spectra of the sample before and after low temperature annealing deposited at T_{fil} = 1800 °C and T_{subs} = 200 °C.

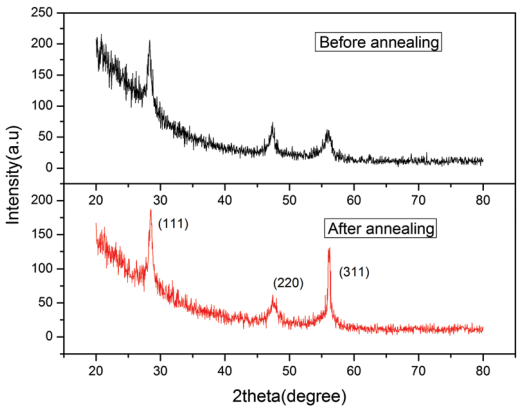

Fig. 4 XRD pattern of the sample prepared at T_{fil} = 1800 °C and T_{subs} = 200 °C, before and after low temperature annealing.

Earlier in one of the reports, the same kind of facet evolution has been reported as a consequence of heating the sample. Together with the surface mass transport and free energy change, the evolution was explained with the resulting stability of the material.[33] The results displayed almost no change in the size or density of QDs nevertheless the phase change at (311) could be due to the stability attained because of low temperature annealing.

SEM and AFM analysis

For the morphological analysis of nanoparticles, SEM analysis has been carried out at different locations of the low temperature annealed sample. Fig. 5 shows the micrographs obtained from the analysis. The differences appearing in the morphology of the sample in two different positions could be clearly seen. Both the micrographs have been obtained at a scale of 100 nm and from Fig. 5(a) it is clear that the grain distribution in the present case is different from the other region shown in Fig. 5(b).

These grain distributions can be responsible for the resulting difference in the internal QD's density distribution and could have consequences in the change in PL emission intensity, as was observed in the laser scanning.

In the same way, atomic force microscopy has been performed for the low temperature annealed sample to gain more details about the morphology on the surface of the thin film that we could associate with the internal morphology. Fig. 6 shows an AFM picture of the nanocrystalline silicon thin film deposited on the silicon substrate.

Analyses were accomplished in the same way as FTIR at dissimilar locations of the sample to observe the morphological changes appearing in the various parts of the sample. Apart from the visible differences (grain distribution and roughness) appearing in the images, more analyses were performed on a constant area of 0.6 μm^2 using the IAP9 software, and the same has been illustrated in Table 1. The variation in the number of grains (28 to 164) and roughness (2.709 nm to 4.997 nm) is clearly visible for the three examined regions.

In the present case, it is seen that before annealing, using a 325 nm laser source (3.8 eV) the as-deposited sample was having only the white-blue emission due to the broad size distribution of the nanoparticles. On the other hand, the intensity was different in different zones of the sample, as it is directly associated with the density (Fig. 5), and good surface passivation of nanoparticles

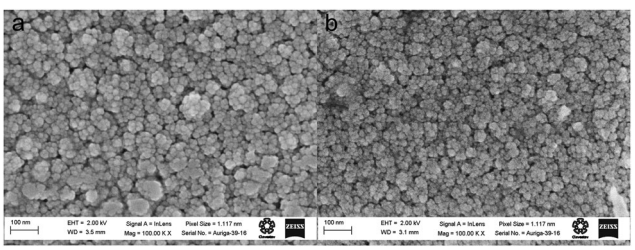

Fig. 5 SEM image of the low temperature annealed sample deposited at T_{subs} = 200 °C and T_{fil} = 1800 °C: (a) corresponds to the left part of the sample whereas, (b) to the right side of the sample.

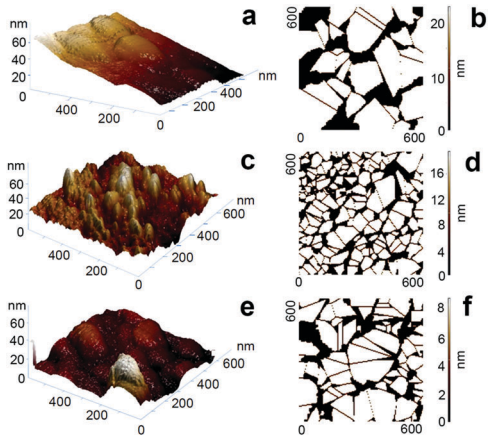

Fig. 6 AFM analysis of the sample after low temperature annealing at three different locations of the sample; (b), (d) and (f) show the grain analysis corresponding to (a), (c) and (e).

Table 1 AFM analysis of the selected area performed using IAP9 software

Sample identification	Number of grains (area of 0.6 μm^2)	Average roughness in nm
Position 1	74	2.709
Position 2	164	4.810
Position 3	28	4.997

with hydrogen or oxygen species. However, as a consequence of low temperature annealing, the probability is that there could be hydrogen effusion on the surface of nanocrystalline particles or from the bulk of the film, which is clearly visible in Fig. 3 (FTIR). Moreover, as evident from all the results obtained (SEM and AFM), it is clear that in different regions of the low temperature annealed sample there exists a different kind of density of nanoparticles. In addition, in Fig. S2 (ESI‡) it can be seen that the thickness of the film before annealing was 680 nm. After low temperature annealing, the thickness remained almost the same without any change in the interference colour (observed by the naked eye). Based on the previous results obtained, it could be confirmed that the hydrogen effusion or oxidation process all together is not enough to generate any measurable differences in the thickness of the films. Even more, the matrix in the present case consists of silicon-oxide, which is thermally very stable and annealing in the presence of nitrogen gas cannot be adequate to produce any modifications in the matrix thickness.

Based on the results obtained we propose a hypothesis depending on the different densities and/or the passivation environment of nanoparticles that could exist in the thin film. If in the case of the region with less density, hydrogen effusion process takes place, it could result in subsequent oxidation of the nanoparticle surface and would result in a blue shift of the PL. On the other hand, in the region, rich in silicon concentration (nanoparticles are highly packed), if the hydrogen effusion process takes place, it would result in the fusion process of the closer nanoparticles, and in that case, it would lead to a redshift of PL. Schematic illustration of the same

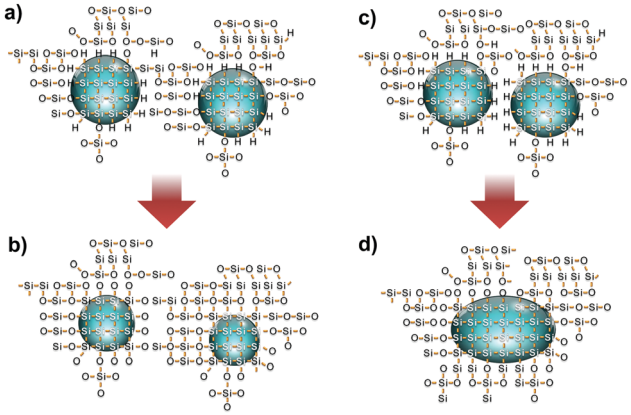

Fig. 7 Schematic illustration (hypothesis) of the aftereffects of the annealing process. (a) Low density of particles separated by the amorphous matrix. (b) Oxidation process of the nanoparticles. (c) High density of particles separated by hydrogen bonding. (d) Effusion process and increment in average size of nanoparticles.

assumption has been presented in Fig. 7. Fig. 7(a) represents the case of low density where two particles are separated by the amorphous matrix. However, because of annealing, the effusion process occurs, and it results in subsequent oxidation as well as in a decrement in the size of nanoparticles, Fig. 7(b). On the other hand, in the case of densely packed nanoparticles, Fig. 7(c), as an outcome of annealing and effusion of hydrogen, it resulted in the overall increment of the size of nanoparticles, Fig. 7(d).

For the confirmation of our hypothesis based on the experimental results obtained, we carried out theoretical simulations (passivation by hydrogen and oxygen species) on different quantum dot sizes (Si_{17} to Si_{87} atoms) and their influence on the band gap tuning.

Surface passivation of QDs

Fig. 8 presents the DOS of the Si_{29} cluster with all hydrogen (H, H, and H) and all oxygen (OH, OH, and OH) surface passivation. The optimized geometries and the HOMO–LUMO are included in the figure. From the cluster structure of Si_{29} and Si_{35}, the loss of symmetry caused by the presence of oxygen on the surface for the Si_{29} cluster can be observed. As a result, the shape of the density of states (DOS) has also been modified. A band gap increase from 1.7 eV (OH, OH, and OH) to 4.4 eV (H, H, and H) is provoked by the different passivation due to the displacement of the valence band edge towards inner energy levels. In the case of the (OH, OH, and OH) cluster, humps and irregularities that can be observed in the conduction band on the (H, H, and H) cluster reveal the difference in the electronic distribution and the electrostatic potential of the cluster, Fig. 8(b) and (c). In concordance with the DOS, the electronic density distribution in the HOMO and the LUMO for the (H, H, and H) cluster shows the changes caused by the presence of oxygen. In the case of the (H, H, and H) cluster, both orbitals are evenly and symmetrically distributed. The transition could occur from the surface silicon atoms to the inner silicon atoms present in the cluster. Contrarily, the HOMO–LUMO transition in the case of the (OH, OH, and OH) cluster reveals more participation of oxygen atoms on silicon atoms at the occupied level. Also, the probable transition could occur from oxygen and silicon atoms on the surface to the inner silicon atoms. These changes are in complete concordance with the results of DOS and with the model explained in Fig. 7.

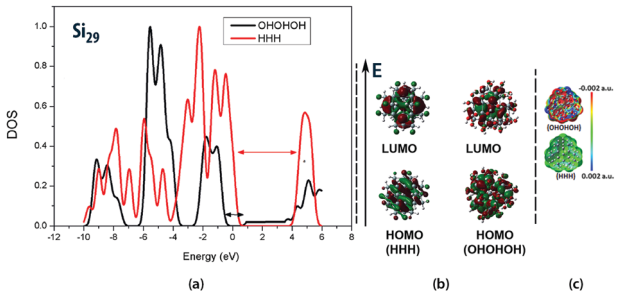

Fig. 8 (a) DOS of the Si_{29} cluster passivated only with H atoms (HHH) or OH groups (OHOHOH), respectively. (b) HOMO and LUMO for (HHH) and (OHOHOH) Si_{29} clusters. (c) The molecular electrostatic potential for (HHH) and (OHOHOH) Si_{29} clusters, respectively.

The frontier molecular orbital diagram for the (H, H, and H) cluster has a triple degenerated HOMO (Fig. S3, ESI‡). Fig. 8(c) shows the electrostatic potential distribution for (H, H, and H) and (OH, OH, and OH) clusters. As can be seen, the presence of oxygen causes more polarization in the charge distribution. On the other hand, the charge distribution is uniform in the case of hydrogen passivation. As a consequence, the (OH, OH, and OH) surface presents the permanent separation of charge. These simulation results demonstrate that irrespective of the change in the size and the density of QDs (cannot occur at low temperature annealing), the surrounding/passivation environment is also very important for the change in the resulting band gap. Hydrogen/oxygen complete or partial passivation could modify the band gap and hence, could lead to the shift from blue to green and then, red luminescence as seen in Fig. 1. Table 2 shows some of the theoretical band gap values obtained from the DOS in Fig. 8 for different passivation environments.

Additionally, there could also be the possibility of the presence of the region with intermediate density levels compared to the two processes mentioned earlier and it could result in green emission (as can be seen in Fig. 1). For a better understanding of the possible growth/reduction in the size of QDs, analysis was performed and is presented in Fig. 9–11.

Size reduction reaction mechanism

In this particular case, when the Si_{17} cluster is in the atmosphere of oxygen atoms, there occurs a process of sub-sequential

Table 2 DFT passivation effect on the band gap (eV) for the Si_{29} cluster

Type of passivation	Calculated band gap value (in eV)
H, H, H	4.4
H, H, OH	3.08
H, OH, OH	2.7
OH, OH, OH	1.7

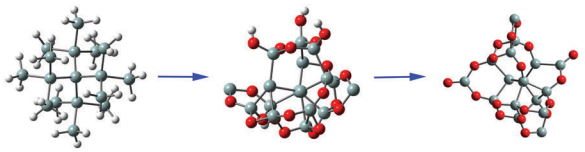

Fig. 9 Reaction mechanisms illustrating the size reduction of Si nanoclusters due to surface oxidation. The optimized structure of $Si_{17}H_{51}$ to $Si_{17}O_{20}H_4$ and then finally $Si_{17}O_{18}$ is presented.

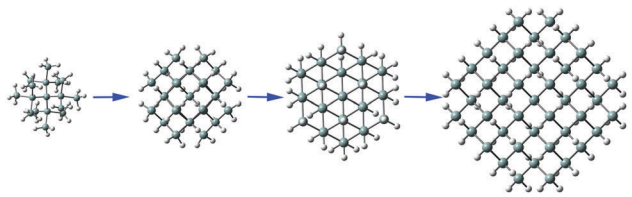

Fig. 10 Reaction mechanism of growth of Si nanoclusters. The optimized structure of $Si_{17}H_{51}$ to $Si_{35}H_{36}$ and then finally $Si_{87}O_{76}$ is presented.

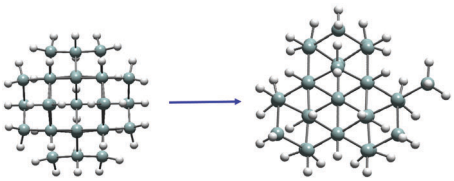

Fig. 11 Optimized structure of $Si_{29}H_{36}$ upon reaction with SiH_3 radical species is presented.

oxidation as observed earlier in Fig. 3. As a whole, this process could decrease the size of the cluster as illustrated in Fig. 7(a) and (b). Moreover, the size reduction is illustrated in Fig. 9, and data are presented in Table 3. In the first step, the hydrogen atoms effusing during annealing are substituted by oxygen. The energy liberated, in that case, is 316.14 eV, which shows the exothermic nature of the process. As can be seen from Table 3, the occupied volume decreased from 630.45 Å^3 to 544.64 Å^3, which shows the decrement in the size of the cluster. For the second step, though the reaction energy is 8.8 eV, this step is endothermic, but this energy can be attained from the thermal energy liberated to the surroundings. On the other hand, the occupied volume decreased from 544.64 Å^3 to 515.86 Å^3 for this reaction step. These two reaction processes show the oxidation of an initially hydrogen rich silicon cluster and the subsequent decrement in size.

Table 3 Respective value of the reactions of the reduction of silicon clusters in eV along with the Connolly surface (occupied volume) in Å^3 is presented

Reaction	ΔE (eV)	Connolly surface (occupied volume) for QDs (initial/final) (Å^3)
$Si_{17}H_{51} + 10\ O_2 \rightarrow Si_{17}O_{20}H_4 + 47/2H_2$	−316.14	630.45/544.64
$Si_{17}O_{20}H_4 \rightarrow Si_{17}O_{18} + 2H_2 + O_2$	8.08	544.64/515.86

Size increment reaction mechanism

In the case of growth of silicon clusters, two different models one presenting an overall increase in size from Si_{17} to Si_{87} and the other with the response of the Si_{29} cluster with only one. SiH_3 radical are presented.

In Fig. 10, we have shown the growth of the Si_{17} cluster in the presence of. SiH_3 radical species. In the first step, the cluster increased from Si_{17} to Si_{29} with an exothermic reaction energy of −259.29 eV (Table 4). The occupied volume increased from 630.45 to 848.65 Å^3. The second step shows the formation of Si_{35} with an energy release of −10.36 eV. The occupied volume for this cluster is 952.66 starting from 848.65 Å^3. In the final step, the cluster increased to Si_{87} with an energy release of −85.51 eV. Ultimately, the occupied volume, in this case, is 2360.36 Å^3. All these reaction processes show the size increment of silicon clusters using the attachment of nearby silicon radicals generated after hydrogen effusion caused by thermal annealing and show good agreement with the assumption shown in Fig. 7(c) and (d).

In Fig. 11, the growth of the Si_{29} cluster in the presence of $^{\bullet}SiH_3$ radical species at the only reactive site is presented, and the results are shown in Table 5. As a result, an increase in the size of the cluster is confirmed by the occupied volume increase from 848.65 to 886.33 Å^3. All the results obtained after low temperature annealing together with the model described in Fig. 7 go well in hand with the simulations and the reaction processes proposed in this work. Hence, depending on the size and/or passivation environment modification in the band gap, a consecutive shift in the luminescence is possible.

Furthermore, to confirm the presence of QDs, TEM measurements have been carried out and are demonstrated in Fig. 12. It can be seen from Fig. 12(a) that the particles are in the size regime of 2–5 nm. On the other hand, the well ordered crystalline nature of the particles can be seen from Fig. 12(b)–(d). It is noteworthy to mention that the particles, in this case, are randomly distributed due to the catalytic reaction of source gases over the hot filament which further depends on the deposition conditions like substrate temperature or position, filament temperature, the substrate to filament distance, *etc.* From the various measurements of the TEM, it can be concluded that there exists a random distribution

Table 4 Exothermic reactions in eV and occupied volume by clusters in Å^3 is presented

Reaction	ΔE (eV)	Connolly surface (occupied volume) for QDs (initial/final) (Å^3)
$Si_{17}H_{51} + 12SiH_3 \rightarrow Si_{29}H_{36} + 51/2H_2$	−259.39	630.45/848.65
$Si_{29}H_{36} + 6SiH_3 \rightarrow Si_{35}H_{36} + 9H_2$	−10.36	848.65/952.66
$Si_{35}H_{36} + 52SiH_3 \rightarrow Si_{87}H_{76} + 58H_2$	−85.51	952.66/2360.36

Table 5 Endothermic reaction in eV and occupied volume by clusters in Å^3

Reaction	ΔE (eV)	Connolly surface (occupied volume) for QDs (initial/final) (Å^3)
$^{\bullet}Si_{29}H_{35} + {}^{\bullet}SiH_3 \rightarrow Si_{29}H_{35}–SiH_3$	14.42	848.65/886.33

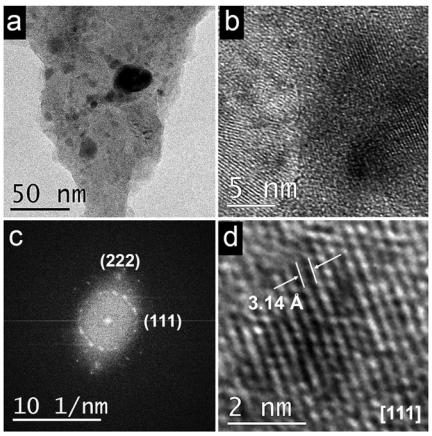

Fig. 12 TEM images of the annealed sample (a) obtained at a scale of 20 nm, (b) obtained at a scale of 5 nm, (c) selected electron diffraction (SAED) pattern and (d) obtained at a scale of 2 nm.

Table 6 Comparison of the size of QDs (nm), PL energy from eqn (1) (eV) and PL spectral values from Fig. 1 (nm and eV)

Size (nm)	PL peak energy (eV) (from eqn (1))	PL peak position (from Fig. 1)
1	5.53	
2	3.22	
3	2.61	470 nm = 2.6 eV
4	2.34	498 nm = 2.44 eV
5	2.19	588 nm = 2.10 eV

of silicon particles embedded in the silicon oxide matrix as demonstrated in Fig. 7(a) and (c) with different depth ranges.

Table 6 shows three essential elements. They are the size (d) of nanoparticles, PL peak values calculated after substituting d values (1 to 5 nm) in eqn (1) and PL peak energy (obtained from the PL spectra in Fig. 1).

Different sizes (d) of QDs are substituted in eqn (1) and further, PL energy values are calculated. A brief comparison has been made between the experimental PL values obtained from Fig. 1 and the PL peak energy value obtained from eqn (1).

It can be seen that the experimental results obtained go well in correlation with the effect of passivation (Table 2) and thus, the band gap of the resulting QDs. This makes sure that in the present case due to annealing, hydrogen effusion causes various surface reactions which lead to a change in the size distribution of QDs in the SiO_x matrix. Additionally, depending on the passivation and the size of QDs, different colour emissions are obtained. All these results confirm the confinement effect on the visible emission.

Furthermore, to have better clarity and validation of the effusion of hydrogen, more results related to the sample annealed at 950 °C (high temperature annealing) for 60 minutes have also been presented. From Fig. 13, the changes appearing in the silicon, hydrogen and oxygen species on the thin film surface as a result of annealing at a higher temperature of 950 °C can be observed. In comparison to the annealing performed at 550 °C (Fig. 3), in this case, the Si–H wagging absorption band at

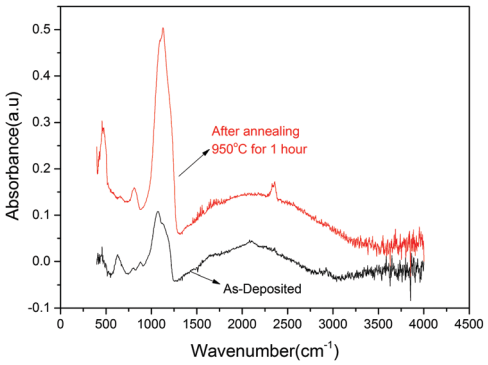

Fig. 13 FTIR spectra of the sample before and after annealing at 950 °C for 60 minutes.

620 cm^{-1} diminished completely. On the other hand, the intensity of the absorption bands related to Si–O out-of-plane rocking, Si–O bending and Si–O stretching in-phase and out-of-phase modes increased significantly. It remarks a more profound effusion process of the hydrogen species as a result of the higher temperature annealing process.

In Fig. 14, PL comparison of the as-deposited sample has been made with the annealed sample, and it can be observed that here as well the as-deposited sample was emitting in the white-blue region. However, because of the higher temperature annealing process on the sample, a marked red shift was observed in the spectrum, and the maximum intensity was found at around 580 nm. When the laser was moved over the surface of the sample, the yellow-orange colour was observed all over.

All these results signify that at a lower annealing temperature of 550 °C, there was a partial effusion process of hydrogen. Moreover, as discussed earlier in that case, as an upshot of the hydrogen effusion process on different sizes and surrounding environments of nanoparticles, we observed different kinds of colour emissions. However, when we increased the annealing temperature to 950 °C for a duration of one hour, there is a more efficient hydrogen effusion process. In particular, this provides sufficient energy for the surface reactions which could result in the fusion of the closest QDs and for the better

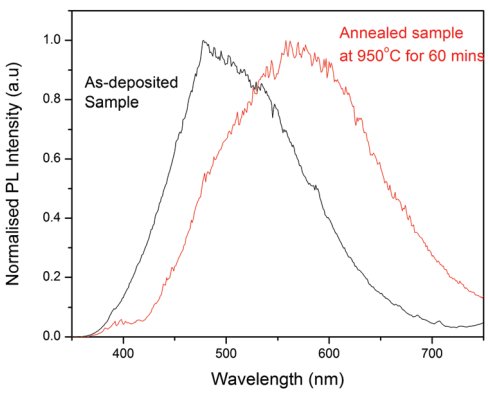

Fig. 14 PL spectra of the sample before and after annealing at 950 °C for 60 minutes.

recrystallization process of the nanoparticles embedded in the matrix as shown in Fig. 7(c), (d), 10 and 11. This process is identical for all over the sample irrespective of the initial lower, medium or higher density of QDs. Finally, this process is generating an overall increase in the average size of QDs and resulted in yellow-orange emission. One way or another, these experiments show the consequence of the QCE in visible emission from nc-Si embedded in SiO_x matrix thin films. Hence, in the present work apart from the explanation of the mechanism of visible luminescence, the potential of this material for the fabrication of LEDs or third generation solar cells based on silicon quantum dots with wide size distribution has been illustrated.

Conclusions

In this work, the luminescence properties of nanocrystalline silicon embedded in the silicon oxide matrix have been explored by combining both experimental and theoretical studies. It has been observed that the initial density of Si QDs affects a lot the physical as well as the optical properties of the thin film. At a lower substrate temperature of 200 °C, the as-deposited sample showed intense white luminescence at room temperature. Annealing performed in a nitrogen atmosphere instigated the hydrogen effusion in the matrix and caused the appearance of various sizes and the change in the surroundings of QDs in the matrix. Likewise, theoretical calculations allowed us to elucidate the surface reactions leading to a size increment or reduction during this process. Apart from that, in this work, we have shown the ideal annealing temperature to obtain homogenous emission from the whole sample in comparison to the as-deposited sample but with a red shift in the luminescence spectra. Based on DFT calculations performed on the Si cluster with 17, 29, 35 and 87 atoms, it was found that depending on the size and passivation of Si QDs, their band gap could vary from 1.7 to 4.4 eV. Similarly, the model explained in this work supports the variation of the band gap from 2–4 eV depending on the size and passivation of QDs. It is conceivable to conclude that in the present work, using HW-CVD, it is possible to achieve visible emission and the mechanism of emission in this circumstance uses the QCE. In addition, the presence of a wide distribution of various sizes of nanoparticles shows the potential use of these materials in the fabrication of LEDs (white light emission from as-deposited samples and red emission after high temperature annealing) or third generation solar cells based on silicon quantum dots. Our study provides the basis for the fabrication of devices with tunable luminescence along with a consistent theoretical explanation of the mechanism.

Acknowledgements

Ateet Dutt acknowledges the DGAPA postdoctoral scholarship and assistance. The authors thank Angela Gabriela López for sample preparations. The authors are indebted to Marcela Guerrero for their technical assistance. We would express our sincere thanks to Josué E. Romero-Ibarra for SEM measurements and C. D. Ramos Vilchis for technical assistance. We also want to acknowledge Gyna Ramirez for her contribution in AFM measurements. This project is supported by the National Council of Science and Technology (CONACyT) No. CB2009-128723 and CB2012-179632. Estrella Ramos acknowledges Alejandro Pompa and Alberto López for technical help and thanks for projecting DGAPA PAPIIT IN109815/27 and RN109815/27.

References

1 L. T. Canham, *Appl. Phys. Lett.*, 1990, **57**(10), 1046–1048.
2 H. Takagi, H. Ogawa, Y. Yamazaki, A. Ishizaki and T. Nakagiri, *Appl. Phys. Lett.*, 1990, **56**(24), 2379–2380.
3 M. Dovrat, Y. Goshen, J. Jedrzejewski, I. Balberg and A. Sa'ar, *Phys. Rev. B: Condens. Matter Mater. Phys.*, 2004, **69**(15), 1–8.
4 L. Spallino, L. Vaccaro, L. Sciortino, S. Agnello, G. Buscarino, M. Cannas and F. M. Gelardi, *Phys. Chem. Chem. Phys.*, 2014, **16**, 22028.
5 X. Chen, C. Li and H. K. Tsang, *NPG Asia Mater.*, 2011, **3**(1), 34–40.
6 F. Erogbogbo, C. W. Chang, J. L. May, L. Liu, R. Kumar, W. C. Law, H. Ding, K. T. Yong, I. Roy, M. Sheshadri, M. T. Swihart and P. N. Prasad, *Nanoscale*, 2012, **4**, 5483–5489.
7 K. Fujioka, M. Hiruoka, K. Sato, N. Manabe, R. Miyasaka and S. Hanada, *Nanotechnology*, 2008, **19**(41), 415102.
8 G. Ledoux, O. Guillois, D. Porterat, C. Reynaud, F. Huisken and B. Kohn, *Phys. Rev. B: Condens. Matter Mater. Phys.*, 2000, **62**(23), 15942–15951.
9 H. Imai, K. Arai, H. Imagawa, H. Hosono and Y. Abe, *Phys. Rev. B: Condens. Matter Mater. Phys.*, 1988, **38**(17), 12772–12775.
10 M. Stapelbroek, D. L. Griscom, E. J. Friebele and G. H. Sigel Jr., *J. Non-Cryst. Solids*, 1979, **32**(1–3), 313–326.
11 S. Munekumi, T. Yamanaka, Y. Shimogaichi, K. Nagasawa and Y. Y. Hama, *J. Appl. Phys.*, 1990, **68**, 1212.
12 E. P. Reilly and J. Robertson, *Phys. Rev. B: Condens. Matter Mater. Phys.*, 1983, **27**, 3786.
13 S. M. Prokes and W. E. Carlos, *J. Appl. Phys.*, 1995, **78**(4), 2671–2674.
14 C. Tsai, K.-H. Li, J. Sarathy, S. Shih, J. C. Campbell and B. K. Hance, *Appl. Phys. Lett.*, 1991, **59**(22), 2814–2816.
15 D. J. Wolford, B. A. Scott, J. A. Reimer and J. A. Bradley, *Physica B+C*, 1983, **117–118**, 920–922.
16 X. D. Pi, R. W. Liptak, J. Nowak Deneen, N. P. Wells, C. B. Carter and S. A. Campbell, *Nanotechnology*, 2008, **19**(24), 245603.
17 Y. Matsumoto, A. Dutt, G. Santana-Rodríguez, J. Santoyo-Salazar and M. Aceves-Mijares, *Appl. Phys. Lett.*, 2015, **106**(17), 171912.
18 A. Dutt, Y. Matsumoto and G. Santana-Rodríguez, *Curr. Nanosci.*, 2015, **11**(5), 621–626.
19 A. Dutt, Y. Matsumoto, J. Santoyo-Salazar, G. Santana-Rodríguez and S. Godavarthi, *Thin Solid Films*, 2015, **595**, 221–225.
20 W. Z. Shen, *Proc. SPIE*, 2010, 79952V.
21 Y. Matsumoto, *Thin Solid Films*, 2006, **501**(1–2), 95–97.
22 W. Kohn and A. D. Becke, *J. Phys. Chem.*, 1996, **100**, 12974–12980.

23 P. Hohenberg and W. Kohn, *Phys. Rev.*, 1964, **136**, B864–B871.
24 W. Kohn and L. Sham, *Phys. Rev.*, 1965, **140**, A1133–A1138.
25 M. J. Frisch, *Gaussian 09, revision A.02*, Gaussian, Inc., Wallingford, CT, 2009.
26 (*a*) J. P. Perdew and Y. Wang, *Phys. Rev.*, 1992, **45**, 13244–13249; (*b*) J. P. Perdew, K. Burke and Y. Wang, *Phys. Rev.*, 1996, **54**, 16533–16539; (*c*) J. P. Perdew, P. Ziesche and H. Eschrig, *Electronic structure of solids' 91*, Akademie Verlag, Berlin, 1991, p. 11.
27 (*a*) R. Krishnan, J. S. Binkley, R. Seeger and J. A. Pople, *J. Chem. Phys.*, 1980, **72**, 650–654; (*b*) A. D. McLean and G. S. Chandler, *J. Chem. Phys.*, 1980, **72**, 5639–5648.
28 A. D. Becke, *J. Chem. Phys.*, 1993, **45**, 5648–5652.
29 E. Ramos, B. M. Monroy, J. C. Alonso, L. E. Sansores, R. Salcedo and A. Martinez, *J. Phys. Chem. C*, 2012, **116**, 3988–3994.
30 M. Connolly, *J. Appl. Crystallogr.*, 1983, **16**, 548–558.
31 K. Tanaka, N. Happo and M. Fujiwara, CAS 2012 (International Semiconductor Conference) *IEEE* 2012, 171–4.
32 M. S. Brandt, H. D. Fuchs, M. Stutzmann, J. Weber and M. Cardona, *Solid State Commun.*, 1992, **81**(4), 307–312.
33 S.-H. Lim, S. Song, G.-D. Lee, E. Yoon and J.-H. Lee, *J. Vac. Sci. Technol., B: Microelectron. Nanometer Struct. – Process., Meas., Phenom.*, 2004, **22**(2), 682–687.